https://doi.org/10.1016/j.applthermaleng.2019.113992

A hybrid system using Brayton cycle to harvest the waste heat from a direct carbon solid oxide fuel cell

Zhimin Yang[1, 2], Houcheng Zhang[1, *], Meng Ni[3], Bihong Lin[4]

[1] *Department of Microelectronic Science and Engineering, Ningbo University, Ningbo 315211, China*

[2] *Department of Physics, Xiamen University, Xiamen 361005, China*

[3] *Department of Building and Real Estate, The Hong Kong Polytechnic University, Hung Hom, Kowloon, Hong Kong, China*

[4] *College of information science and engineering, Huaqiao University, Xiamen 361021, China*

Abstract: A new hybrid system model is developed to evaluate the potentials of a Brayton cycle heat engine for waste heat recovery from a direct carbon solid oxide fuel cell (DC-SOFC). The maximum power density of the proposed system is up to 0.8675 Wcm^{-2}, which is approximately 1.8 times as large as that of the single DC-SOFC. Numerical calculations also indicate that the proposed hybrid system is an efficient approach to boost the fuel utilization, and the maximum power density of the proposed system is markedly better than that of the DC-SOFC/thermophotovoltaic cell, DC-SOFC/thermionic generator, and DC-SOFC/Otto heat engine hybrid systems except for the DC-SOFC/Stirling engine hybrid system. The optimum regions for power density, efficiency and operating current density of the proposed system are determined. The higher operating temperature and lower gap between the anode and carbon layer increase the power density and efficiency of the proposed system. Moreover, the higher heat transfer coefficient boosts the power density and efficiency at high current density. The compression efficiency, expansion efficiency and recuperator coefficient significantly affect the power density and efficiency.

Keywords: Brayton cycle, Direct carbon solid oxide fuel cell, Hybrid system, Optimum working region, maximum power density

* Corresponding author. Email address: zhanghoucheng@nbu.edu.cn (H. Zhang).

1. Introduction

Fuel cells are electrochemical devices that directly convert chemical energy of fuels into electrical energy [1], and they are one of the most promising energy conversion technologies owing to their unique merits such as high efficiency, cleanliness and silent operation [2, 3]. Based on the types of electrolytes, fuel cells can be classified into the following categories [1, 4]: polymer electrolyte membrane fuel cell (PEMFC), high temperature PEMFC, direct methanol fuel cell (DMFC), molten carbonate fuel cell (MCFC), phosphoric acid fuel cell (PAFC), solid oxide fuel cell (SOFC), and alkaline fuel cell (AFC). Most of these kinds of fuel cells are fed with hydrogen. However, the generation and storage of hydrogen still suffer from several technology problems [5]. Therefore, people resort to find some cheap and abundant alternative fuels such as carbon, methane and natural gas [6].

A direct carbon fuel cell (DCFC) is a kind of fuel cells that employs carbon as fuel [5, 7], which provide advantages such as high theoretical thermal efficiency, abundant and cheap fuels and convenient CO_2 sequestration [8, 9]. DCFCs can be mainly classified into three types based on the electrolyte categories including molten hydroxide, molten carbonate, and solid oxide DCFCs [10]. Compared with other types, direct carbon solid oxide fuel cells (DC-SOFCs) are whole-solid state devices that avoid electrolyte degradation and leakage problems and offer significant advantages, such as fast electrochemical processes, concentrated CO_2 product streams and high-quality waste heat for combined heat and power (CHP) applications [11]. To enhance the DC-SOFC performance, most of the endeavors are made on electrolytes [12], fuels [13], catalysts [14], physical/chemical processes [15], electrodes [16], thermal management [17], and prototypes [18, 19]. Alternatively, harvesting the waste heat for additional power generation is also an alternative approach to improve the DC-SOFC performance [20, 21]. A number of thermal devices can serve as the bottoming cycles for the topping fuel cells, including the thermoelectric generator (TEG) [22], vacuum thermionic generator (VTIG) [23],

thermophotovoltaic cell (TPVC) [24], Brayton cycle [25], Stirling cycle [26], Braysson cycle [27, 28], heat engine [29], thermally regenerative electrochemical cycle (TREC) [30] and Rankine cycle [31]. Amongst, the Brayton cycles are much closer to practical applications owing to their compactness, maturity and lower cost [32]. The Brayton cycles have been extensively utilized in many areas such as waste heat recovery [33], nuclear energy [34], concentrated solar power [35], and coal-fired power plants. The Brayton cycles have been widely used as the bottoming or intermediate cycles for SOFCs and MCFCs. For example, Huang et al. [36] proposed a hybrid system consisting of the SOFC, Carnot cycle, and Brayton cycle and analyzed the effects of the operating temperature, fuel flow rate, and hydrogen utilization on the power density and efficiency of the hybrid system. Pirkandi et al. [37] presented the thermo-economic analyses for four different configurations of a solid oxide fuel cell/gas turbine system and determined the optimum configuration. Sánchez et al. [38] compared the MCFC combined with the supercritical carbon dioxide and air Brayton cycles. Obviously, the Brayton cycles can be readily used to harvest the waste heat generated by the DC-SOFCs and thus the advantages for the DC-SOFCs could be further reinforced. However, few studies regarding DC-SOFC/Brayton cycle hybrid system have been reported in the current literatures. Compared with the previous studies on the fuel cells/Brayton cycle hybrid systems, a more accurate model of the topping DC-SOFC is adopted, in which the electrochemical/chemical reactions, ionic/electronic charge transport, mass/momentum transport, and heat transfer are considered. Moreover, the maximum power densities for the available DC-SOFC-based hybrid systems are compared.

In this study, a Brayton cycle heat engine is proposed to recover the possible waste heat from a DC-SOFC. The thermal characteristics of the DC-SOFC are solved using the finite element method, from which the integration and assessment of the hybrid system will be demonstrated. The effectiveness and feasibility of this hybrid system will be shown by

77 comprehensive comparisons. Comparisons between the proposed hybrid system and the stand-
78 alone DC-SOFC will be performed to evaluate the effectiveness of the proposed hybrid system.
79 The feasibility will be justified by comparing the performance improvements of several
80 existing waste heat recovery technologies. Meanwhile, the dependence of the hybrid system
81 performance on some design parameters and operating conditions will be revealed through
82 comprehensive parametric studies.

83 **2. Model description**

84 Figure 1 illustrated the energy-flow sketch of the DC-SOFC/ Brayton cycle heat engine hybrid
85 system. It is seen that the hybrid system is mainly composed of a DC-SOFC, a Brayton cycle
86 heat engine, an external heat source, and a regenerator. q_{E} is the heat flow provided to the
87 DC-SOFC from the external heat source if necessary; q_{h} is the heat flow generated in the DC-
88 SOFC and transferred to the Brayton cycle heat engine at large operating current densities;
89 q_{Loss} is the heat loss from the DC-SOFC to the environment; q_l is the heat flow from the
90 Brayton cycle heat engine to the environment; P_{f} and P_{B} are, respectively, the power outputs
91 of the DC-SOFC and the Brayton cycle, and T_0 is the ambient temperature. When the DC-
92 SOFC works at a low current density, the heat resulted from the electrochemical reaction and
93 overpotential losses is less than the heat demand by the Boudouard reaction. In this situation,
94 the external heat source should provide an amount of heat q_{E} to the DC-SOFC for ensuring
95 its normal operation. When the DC-SOFC runs at a high current density, the heat released in
96 the cell could be larger than the heat demand by the Boudouard reaction. In this situation, the
97 excessive heat q_{h} is collected and transferred to drive the Brayton cycle for additional power
98 generation. As a result, the performance of the hybrid system can be improved. The regenerator
99 is used to preheat the input reactants to reach the working temperature of the DC-SOFC with
100 the assistance of the high-temperature exhaust gases. The DC-SOFC and Brayton cycle heat

engine are connected indirectly, and there is only heat exchange instead of mass exchange between the DC-SOFC and the Brayton cycle heat engine.

a) The DC-SOFC

The DC-SOFC model is adopted from Refs. [15, 39]. As illustrated in Fig. 2, the 2D tubular DC-SOFC mainly includes two electrodes, an electrolyte and gas channels, where d is the distance between the anode and the carbon layer. The DC-SOFC operates as a carbon internal dry reforming SOFC as per the "CO shuttle" mechanism. The solid carbon (C) reacts with initial oxygen (O_2) to produce carbon dioxide (CO_2) in the anode chamber, and the produced CO_2 reacts with the solid carbon to generate carbon monoxide (CO) via the Boudouard reaction (i.e., $C+CO_2 \rightarrow 2CO$). The generated CO is electrochemically oxidized by the O^{2-} at the triple phase boundaries (TPBs) to produce CO_2 and electrons. The produced CO_2 flows back into the anode chamber and reacts with the carbon to produce CO via the Boudouard reaction. The generated electrons arrive the cathode via the external electric circuit and react with O_2 to produce O^{2-}. The electrochemical reactions can be summarized as follows.

Anode reaction: $CO+O^{2-} \rightarrow CO_2+2e^-$ (1)

Cathode reaction: $0.5O_2+2e^- \rightarrow O^{2-}$ (2)

Overall reaction: $C+O_2 \rightarrow CO_2$ (3)

The power output P_f and the efficiency η_f of the DC-SOFC are, respectively, given by

$$P_f = i_f A_f V_f, \tag{4}$$

and

$$\eta_f = \begin{cases} \dfrac{P_f}{q_E + P_f}, i_f < i_q \\ \dfrac{P_f}{q_r + P_f}, i_f > i_q \end{cases}, \tag{5}$$

where i_f is the current density, A_f is the electrode area, and V_f is the output voltage, i_q is the critical operating current density that the heat demand by the Boudouard reaction is satisfied

by the heat released in the SOFC. The heat rejection rate from the DC-SOFC, q_r, is the difference between q_t resulted from the electrochemical reaction and overpotential losses and q_b required by the Boudouard reaction [39], i.e.,

$$q_r = q_t - q_b, \tag{6}$$

where $q_t = \left[-T_f \Delta S/(2F) + (V_{act} + V_{ohm})\right] i_f A_f$, F is the Faraday's constant, T_f is the operating temperature of the DC-SOFC, and ΔS is the molar entropy change of the electrochemical reactions.

The governing equations for the DC-SOFC model are listed in Table 1 [15] and can be solved by the finite element method using commercial COMSOL MULTIPHSICS® based on the parameters summarized in Table 2 [15, 40]. The heat flux $q_r^* = q_r / A_f$ from the DC-SOFC under different operating temperatures are shown in Fig. 3, where i_q is the operating current density at which q_t equals q_b, i.e., $q_r^* = 0$. As seen in Fig. 3, when $i_f < i_q$ (i.e., $q_t < q_b$), some heat should be provided to the DC-SOFC from the external heat source to ensure the DC-SOFC normal operation. When $i_f > i_q$ (i.e., $q_t > q_b$), the excessive waste heat released from the DC-SOFC is transferred to drive the Brayton cycle for additional power generation. It is also seen that q_r^* is increased as i_f increases. Moreover, q_r^* decreases while i_q increases as the fuel cell operating temperature T_f increases.

b) The Brayton cycle

The Brayton cycle model is adopted from Refs. [36, 42]. As shown in Fig. 1, the Brayton cycle heat engine consists of a compressor (C), a turbine (T), a recuperator (REC), and two heat exchangers (i.e., HE1 and HE2). Working substance with low pressure and temperature enters the compressor at state 1 and is compressed. The compressed working substance flows into the recuperator and is heated to a temperature of T_5. The heated working substance is further heated by absorbing the heat q_h generated in the DC-SOFC through the HE1.

Afterwards, the high-pressure and high-temperature working substance enters the turbine and expands to produce power. The exhaust gas of the turbine is used to preheat the inlet working substance through the recuperator and further cooled down after passing through HE2. The leaving working substance with low pressure and temperature enters the compressor to complete the cycle. The $T-S$ diagram of the Brayton cycle is shown in Fig. 4, where T_i ($i=1, 2, 2s, 3, 4, 4s, 5 \text{ or } 6$) is the temperature of the working substance at operating state i, $1\to 2$ and $3\to 4$ are two irreversible adiabatic processes, $1\to 2s$ and $3\to 4s$ are, respectively, the corresponding reversible adiabatic processes.

Assuming that the heat transfer obeys Newton's law, the heat flow from the DC-SOFC to the Brayton cycle is given by [42]

$$q_h = C\dot{m}\varepsilon_h (T-T_5) = C\dot{m}(T_3-T_5) = h_h A_h (T_3-T_5) \Big/ \left(\ln\frac{T-T_5}{T-T_3}\right), \tag{12}$$

where T is the temperature of the heat source, h_h and A_h are, respectively, the heat transfer coefficient and heat transfer area between the heat source and working substance, and ε_h is the hot side coefficient. The heat flow from the Brayton cycle to the environment is given by

$$q_l = C\dot{m}\varepsilon_L (T_6-T_0) = C\dot{m}(T_6-T_1), \tag{13}$$

where C is the heat capacity, $\dot{m}$ is the mass flow rate, ε_L is the cold side coefficient. The compression and expansion efficiencies are introduced to describe the irreversibility of these processes, i.e.,

$$\eta_c = \frac{T_{2s}-T_1}{T_2-T_1}, \tag{14}$$

and

$$\eta_e = \frac{T_3-T_4}{T_3-T_{4s}}, \tag{15}$$

and both η_c and η_e are ranged from 0 to 1. When $\eta_c=\eta_e=1$, it means that the two adiabatic processes are reversible [43]. According to the characteristics of the reversible adiabatic

processes, we have [36, 42]

$$\left(\frac{T_{2s}}{T_1}\right)=\left(\frac{T_3}{T_{4s}}\right)=\left(\frac{p_{\mathrm{B1}}}{p_{\mathrm{B2}}}\right)^{(k-1)/k}=x, \tag{16}$$

where p_{B1} and p_{B2} are, respectively, the pressures at the processes of $2\to3$ and $1\to4$, k is the ratio of specific heats. Based on Eqs. (12)-(16), T_2 and T_4 can be, respectively, expressed as

$$T_2=T_1\left(\frac{x-1}{\eta_c}+1\right), \tag{17}$$

and

$$T_4=T_3\left[1-\eta_e\left(1-\frac{1}{x}\right)\right]. \tag{18}$$

The temperatures T_1, T_3, T_5, and T_6 can be, respectively, expressed as [36, 44]

$$T_1=\varepsilon_L T_0+(1-\varepsilon_L)T_2\varepsilon_{rc}+(1-\varepsilon_L)(1-\varepsilon_{rc})T_4, \tag{19}$$

$$T_3=\varepsilon_h T+(1-\varepsilon_{rc})T_4\varepsilon_{rc}+(1-\varepsilon_{rc})(1-\varepsilon_{rc})T_2, \tag{20}$$

$$T_5=T_4\varepsilon_{rc}+(1-\varepsilon_{rc})T_2, \tag{21}$$

and

$$T_6=T_2\varepsilon_{rc}+(1-\varepsilon_{rc})T_4, \tag{22}$$

where ε_{rc} is the recuperator coefficient.

Combining Eqs. (17), (19) and (22), we can obtain the relationship between T_4 and T_1, i.e.,

$$T_4=\frac{T_1-\left[\varepsilon_L T_0+\varepsilon_{rc}T_1(1-\varepsilon_L)\left(\frac{x-1}{\eta_c}+1\right)\right]}{(1-\varepsilon_{rc})(1-\varepsilon_L)}. \tag{23}$$

Substituting Eqs. (17) and (23) into Eqs. (20) and (21), the relationship between T_3 and T_1 as well as the relationship between T_5 and T_1 can be, respectively, given by

191 $$T_3=\varepsilon_h T+T_1\left(\frac{x-1}{\eta_c}+1\right)(1-\varepsilon_{rc})(1-\varepsilon_h)+\varepsilon_{rc}(1-\varepsilon_h)\left\{\frac{T_1-\left[\varepsilon_L T_0+\varepsilon_{rc}T_1(1-\varepsilon_L)\left(\frac{x-1}{\eta_c}+1\right)\right]}{(1-\varepsilon_{rc})(1-\varepsilon_L)}\right\}, \quad (24)$$

192 and

193 $$T_5=\left[1-\eta_e\left(1-\frac{1}{x}\right)\right]\varepsilon_{rc}\varepsilon_h T+T_1\left(\frac{x-1}{\eta_c}+1\right)\left[1-\eta_e\left(1-\frac{1}{x}\right)\right](1-\varepsilon_{rc})(1-\varepsilon_h)\varepsilon_{rc}+$$
$$\left\{\frac{T_1-\left[\varepsilon_L T_0+\varepsilon_{rc}T_1(1-\varepsilon_L)\left(\frac{x-1}{\eta_c}+1\right)\right]}{(1-\varepsilon_{rc})(1-\varepsilon_L)}\right\}\left[1-\eta_e\left(1-\frac{1}{x}\right)\right]\varepsilon_{rc}\varepsilon_{rc}(1-\varepsilon_h)+(1-\varepsilon_{rc})\left(\frac{x-1}{\eta_c}+1\right)T_1. \quad (25)$$

194 Combining Eqs. (16) and (18), T_{4s} can be expressed as

195 $$T_{4s}=T_3-\frac{T_3-T_4}{\eta_e}. \quad (26)$$

196 Substituting Eqs. (24) and (26) into $T_3/T_{4s}=x$, the relationship between T_1 and x is

197 determined by

198 $$x=\frac{\varepsilon_h\eta_e T+\eta_e T_1\left(\frac{x-1}{\eta_c}+1\right)(1-\varepsilon_{rc})(1-\varepsilon_h)+\varepsilon_{rc}\eta_e(1-\varepsilon_h)f_2}{(\eta_e-1)\left\{\varepsilon_h T+T_1\left(\frac{x-1}{\eta_c}+1\right)(1-\varepsilon_{rc})(1-\varepsilon_h)+\varepsilon_{rc}(1-\varepsilon_h)f_2\right\}+f_2}, \quad (27)$$

199 where $f_1=\left[\varepsilon_L T_0+\varepsilon_{rc}T_1(1-\varepsilon_L)\left(\frac{x-1}{\eta_c}+1\right)\right]$, and $f_2=\frac{T_1-f_1}{(1-\varepsilon_{rc})(1-\varepsilon_L)}$.

200 Thus, the efficiency η_B and the power output P_B of the Brayton cycle can be,

201 respectively, given by

202 $$\eta_B=1-\frac{q_l}{q_h}=1-\frac{T_6-T_1}{T_3-T_5}=1-\frac{T_1\left(\frac{x-1}{\eta_c}+1\right)\varepsilon_{rc}+(1-\varepsilon_{rc})\left[1-\eta_e\left(1-\frac{1}{x}\right)\right]\left[T_5(1-\varepsilon_{rc})+\varepsilon_h T\right]-T_1}{\varepsilon_h T-\varepsilon_{rc}T_5}, \quad (28)$$

203 and

204 $$P_B=q_h-q_L=q_h\eta_B. \quad (29)$$

205 **c) The performance of the hybrid system**

206 Assuming the heat dissipated from the DC-SOFC to the environment obeys radiative and

convective laws, the net heat flow transferred to the Brayton cycle heat engine is given by

$$q_{\mathrm{n}} = q_{\mathrm{r}} - q_{\mathrm{Loss}}, \tag{30}$$

where $q_{\mathrm{Loss}} = (A_{\mathrm{f}} - A_E)[h_{\mathrm{Loss}}(T_{\mathrm{f}} - T_0) + \zeta\delta(T_{\mathrm{f}}^4 - T_0^4)]$ is heat flow rejected from the DC-SOFC into the ambience, h_{Loss} is the convention heat transfer coefficient, A_E is the front area of the heat exchanger 1, δ is the Stefan-Boltzmann constant, and ζ is the emissivity of the DC-SOFC.

The DC-SOFC acts as the heat source of the Brayton cycle with the assumption that the temperature of the heat transferred to the Brayton cycle is the same as the operating temperature of the fuel cell i.e., $T = T_{\mathrm{f}}$. Combining Eq. (12) and Eq. (30), the mathematical relationship between x and i_{f} is given by the following formula:

$$\frac{q_{\mathrm{n}}}{h_h A_h} = \frac{\varepsilon_h T - \varepsilon_{rc} T_5}{\ln \dfrac{T - T_5}{T - T_5(1-\varepsilon_{rc}) - \varepsilon_h T}}. \tag{31}$$

Eq. (31) can be explicitly rewritten as

$$q_r^* - (1-b)[h_{Loss}(T_{\mathrm{f}} - T_0) + \zeta\delta(T_{\mathrm{f}}^4 - T_0^4)] = \frac{\varepsilon_h T - \varepsilon_{rc} T_5}{\ln \dfrac{T - T_5}{T - T_5(1-\varepsilon_{rc}) - \varepsilon_h T}} a, \tag{32}$$

where $q_r^* = q_r / A_{\mathrm{f}}$, $a = k_h A_h / A_{\mathrm{f}}$, $b = A_E / A_{\mathrm{f}}$, and $\zeta\delta T_0^3 / h_{\mathrm{Loss}} = 1.5$ [39].

Considering the contribution of the bottoming Brayton cycle heat engine, the power output P and efficiency η of the hybrid system can be, respectively, expressed as

$$P = P_{\mathrm{f}} + P_{\mathrm{B}}, \tag{33}$$

and

$$\eta = \frac{P}{q_{\mathrm{r}} + P_{\mathrm{f}}}. \tag{34}$$

d) Model validation

An up-to-date literature survey shows that there is no experimental investigation reported on this specific hybrid system. Based on the parameters used in the DC-SOFC and Brayton cycle as summarized in Tables 2 and 3, the DC-SOFC and Brayton cycle models can be

validated. The DC-SOFC model has been validated in Refs. [15] and [39]. Ref. [39] had shown that the modeling results were in good agreement with the experimental data from Ref. [45], suggesting that the DC-SOFC model could accurately predict the performance of the DC-SOFC. Based on Refs. [25], [42] and [44], the expressions of the efficiency and power output for the Brayton cycle can be derived. To validate the Brayton cycle model, the efficiency of the Brayton cycle is compared with that derived from Sánchez et al. [38], as shown in Fig. 5. Fig. 5 shows that the efficiencies difference between the present Brayton cycle model and the referred model is negligible small, indicating that the present Brayton cycle model is valid and reliable.

3. Results and Discussion

According to the parameter summarized in Table 2 and 3, the numerical study is carried out to predict the performance of the hybrid system. It is observed from Fig. 6 that x and T_1 monotonically increase as i_f increases. This is because the heat generated by the DC-SOFC increases as i_f increases, which results in a variation of T_5, as shown by Eq. (32).

The curves of the efficiencies (η_f, η_B, and η) and the power densities ($P_f^* = P_f/A_f$, $P_B^* = P_B/A_f$, and $P^* = P/A_f$) for the DC-SOFC, Brayton cycle, and hybrid system are shown in Fig. 7, where i_s is the starting operating current density from which the Brayton cycle begins to work, P_m^* and $P_{f,m}^*$ are, respectively, the maximum power densities for the hybrid system and the DC-SOFC, i_P and $i_{f,P}$ are, respectively, the current densities at P_m^* and $P_{f,m}^*$, η_P and $\eta_{f,P}$ are, respectively, the efficiencies of the hybrid system and the DC-SOFC at P_m^* and $P_{f,m}^*$. Fig. 7 shows that when i_f is larger than i_s, both η_f and η monotonically decrease with increasing i_f, while P_f^* and P^* first increase and then decrease with optimum operating current densities at which P_m^* and $P_{f,m}^*$ can be achieved. Moreover, η and P^* are markedly higher than η_f and P_f^*, especially at high current densities. It shows that the

Brayton cycle is effective to recover the waste heat from the DC-SOFC for additional power generation. For the parameters given in Table 1, numerical calculations show that P_m^* with value of 0.8675 W cm^{-2} is attained at a i_f of 3.275 A cm^{-2}, while $P_{f,m}^*$ with value of 0.4773 W cm^{-2} is achieved at a i_f of 2.06 A cm^{-2}. P_m^* is approximately 81.8% larger than $P_{f,m}^*$. Furthermore, η_P and $\eta_{f,P}$ are 65.29% and 50.61%, respectively.

Fig. 8 shows that P^* continuously decreases as η is increased from η_P, and vice versa. P^* and η are two objective functions that conflict with each other. How to make trade-offs between them is an important problem for optimizing the whole system. A simple and available method is to introduce a new objective function that simultaneously considers P^* and η, such as efficient power [46, 47]. The efficient power is defined as the product of the power output and efficiency, i.e., $P \times \eta$. The point D on the $P^* \sim \eta$ curve corresponds to the special case that the efficient power $(P \times \eta)$ achieves its maximum value, where P_D^* and η_D are P^* and η at the point D, respectively. When $\eta < \eta_P$, P^* increases as η increases. When $\eta > \eta_D$, both ηP^* and P^* decrease as η increases. Therefore, the operating regions for P^*, η and i_f can be, respectively, determined as

$$P_D^* \le P^* \le P_m^*, \tag{35}$$

$$\eta_D \ge \eta \ge \eta_P, \tag{36}$$

and

$$i_{f,D} \le i_f \le i_{f,P}, \tag{37}$$

where $i_{f,D}$ is the operating current density at the point D.

T_f not only affects the DC-SOFC performance but also affects the amount of the heat released from the DC-SOFC. The DC-SOFC performance is improved as T_f is increased since the Boudouard reaction kinetics, electrochemical reaction kinetics and ionic conduction are all improved at a higher T_f. In addition, the amount of the heat released from the DC-SOFC is

277 reduced as T_f is increased. The effects of T_f on P^* and η are displayed in Fig. 9, where
278 $d = 59\,\mu\text{m}$ and $a = 60\,\text{W m}^{-2}\,\text{K}^{-1}$. Fig. 9 shows that both P^* and η are improved as T_f
279 increases. Moreover, the critical current density i_q and the starting current density i_s shift
280 rightward with an increase in T_f because the heat generated at the higher temperature is less
281 than that at the lower temperature. However, P_f^* significantly increases as T_f increases. As a
282 result, both P^* and η are obviously promoted with an increase in T_f.

283 The fuel carbon monoxide (CO) concentration and the solid carbon consumption rate of
284 the DC-SOFC are closely related with d. CO is produced from the Boudouard reaction and
285 then consumed by the electrochemical reaction in the porous anode. When d is small, the CO
286 fraction in the porous anode is high. As d increases, the transport of CO from the carbon
287 chamber to the porous anode becomes more difficult, and therefore, the CO fraction in the
288 porous anode decreases as d increases [15]. As seen from Fig. 10, both P^* and η are
289 improved as d decreases because the DC-SOFC performs better at a smaller distance which
290 benefits the CO concentration. The effects of d is initiated from i_s and become strong as i_f
291 increases. Moreover, the values of i_q and i_s get larger as d decreases.

292 Fig. 11 shows both P^* and η increase with the increase of a in a wide range of high
293 current densities. A higher a results in a smaller thermal resistance in the heat-transfer process
294 between DC-SOFC and Brayton cycle heat engine, which in return yields a higher power output
295 for the bottoming Brayton cycle heat engine.

296 To further reveal the influence of the Brayton cycle performance on the overall performance
297 of the hybrid system, the effects of the compression efficiency η_c and expansion efficiency
298 η_e as well as the recuperator coefficient ε_{rc} on P^* and η are discussed. The performance
299 of the DC-SOFC/ Brayton cycle hybrid systems with different η_c, η_e and ε_{rc} are shown in
300 Fig. 12. It is shown that both P^* and η would be enhanced if a higher η_c, η_e or ε_{rc} is

chosen. This result suggests that the performance of the DC-SOFC/ Brayton cycle hybrid system has the potential to be further improved. Fig. 13 compares the DC-SOFC-based hybrid systems available in literatures. It is seen that P_m^* of the DC-SOFC/ Brayton cycle hybrid system is smaller than that of the DC-SOFC/Stirling cycle hybrid system, but it is higher than that of the DC-SOFC/TPVC, DC-SOFC/VTIG, and DC-SOFC/Otto heat engine hybrid systems in a wide temperature span. Due to the disadvantages of the low power/weight ratio, unchanging torque and power swiftly, and high cost of Stirling cycle [48], the Brayton cycle can be still deemed as a competitive alternative for waste heat recovery from the DC-SOFCs. In an actual case, the economic feasibility of the DC-SOFC/Brayton cycle hybrid system should be carefully considered with respect to that of the DC-SOFC. The introduction of Brayton cycle would lead to the increase of investment and running costs. However, the cost increases can be easily recovered by the efficiency gain for a long running time.

4. Conclusions

The hybrid system consisting of the DC-SOFC and the Brayton cycle heat engine is proposed to utilize the waste heat released from the 2D tubular DC-SOFC. The overall heat released in the DC-SOFC can be lower than, equal to or higher than the heat demand by the Boudouard reaction, and consequently, how to operate and evaluate the hybrid system are stated in detail. Compared with the stand-alone DC-SOFC with a maximum power density of 0.4773 Wcm^{-2}, the hybrid system can achieve a higher maximum power density of 0.8675 Wcm^{-2}. The maximum attainable power density of the DC-SOFC/ Brayton cycle hybrid system is higher than that of the DC-SOFC/TPVC, DC-SOFC/VTIG, and DC-SOFC/Otto heat engine hybrid systems except for the DC-SOFC/Stirling cycle hybrid system. The Brayton cycle can be treated as a competitive alternative waste heat recovery technology for DC-SOFCs. The optimal operating regions of the power density, efficiency and current density are determined through introducing a new objective function that simultaneously considers the power density

and efficiency. In addition, the influences of the working temperature of the DC-SOFC, distance between the anode and carbon layer, heat transfer coefficient, compression efficiency, expansion efficiency and recuperator coefficient on the performance of the hybrid system are discussed in detail. A higher operating temperature of the DC-SOFC or a lower distance between the anode and the carbon layer induces a better performance of the combined system. A higher compression efficiency, a larger expansion efficiency or a greater recuperator coefficient can also enhance the combined system performance. Moreover, the maximum power density of the hybrid system can be improved by designing a higher parameter *a*. The results obtained are helpful for the design and operation of such a DC-SOFC/ Brayton cycle hybrid system.

337 **Acknowledgments**

338 This work has been supported by the National Natural Science Foundation of China (Grant No.

339 51406091), the K. C. Wong Magna Fund in Ningbo University, and the Natural Science

340 Foundation of Fujian Province (No. 2016J01021), People's Republic of China.

341

342 Nomenclature

a	Heat transfer coefficient between DC-SOFC and Brayton cycle heat engine, $\mathrm{W\,m^{-2}K^{-1}}$
A_E	Front area of the heat exchanger, $\mathrm{m^2}$
A_f	Electrode area, $\mathrm{m^2}$
A_h	Heat transfer area between the heat source and working substance, $\mathrm{m^2}$
B_0	Permeability, $\mathrm{m^2}$
C	Heat capacity, $\mathrm{J\,Kg^{-1}\,K^{-1}}$
C_p	Heat capacity of fluid, $\mathrm{J\,K^{-1}}$
C_{CO_2}	Molar concentration of CO_2, $\mathrm{Kg\,mol\,m^{-3}}$
d	Distance between the anode and the carbon layer, m
D_j^{eff}	Effective diffusion coefficient of species j, $\mathrm{m^2\,s^{-1}}$
E_{CO}	Equilibrium potential, V
E_{CO}^0	Standard potential, V
E_{rb}	Activation energy of Boudouard reaction, $\mathrm{kJ\,mol^{-1}}$
F	Faraday's constant, $\mathrm{J\,mol^{-1}}$
h_{Loss}	Heat conduction/convection coefficient, $\mathrm{W\,m^{-2}K^{-1}}$
h_h	Heat transfer coefficient between the heat source and working substance, $\mathrm{W\,m^{-2}K^{-1}}$
i_0	Exchange current density, $\mathrm{A\,m^{-2}}$
i_f	Current density of DC-SOFC, $\mathrm{A\,m^{-2}}$
i_s	Starting operating current density, $\mathrm{A\,m^{-2}}$
i_q	Critical operating current density, $\mathrm{A\,m^{-2}}$
k	Ratio of specific heats
k_{rb}	Equilibrium constant of Boudouard reaction, $\mathrm{s^{-1}}$
$\dot{m}$	Mass flow rate, $\mathrm{Kg\,s^{-1}}$
n	Number of electrons transferred
N_i	Flux of mass transport, $\mathrm{Kg\,m^{-3}s^{-1}}$
P	Power output of the hybrid system, W
P^*	Power density of the hybrid system, $\mathrm{W\,m^{-2}}$
P_B	Power output of the Brayton cycle, W
P_B^*	Power density of the Brayton cycle, $\mathrm{W\,m^{-2}}$
P_f	Power output of the DC-SOFC, W
P_f^*	Power density of the DC-SOFC, $\mathrm{W\,m^{-2}}$
p	Partial pressure, Pa
p_{B1}	Pressure at the processes of $2\rightarrow3$ in Brayton cycle, Pa
p_{B2}	Pressure at the processes of $1\rightarrow4$ in Brayton cycle, Pa
$\dot{q}$	Heat consumption or generation, $\mathrm{J\,s^{-1}}$
q_1	Heat flow resulted from the electrochemical reaction and overpotential losses, W
q_b	Heat flow required by the Boudouard reaction, W
q_E	Heat flow provided to the DC-SOFC from the external heat source, W
q_h	Heat flow generated in the DC-SOFC and transferred to the Brayton cycle heat engine, W
q_l	Heat flow from the Brayton cycle heat engine to the environment, W
q_r	Heat flow rejected from the DC-SOFC, W

q_r^*	Heat flux from the DC-SOFC q_r / A_f, $\mathrm{W\,m^{-2}}$
q_{Loss}	Heat loss from the DC-SOFC to the environment, W
R	Gas constant, $\mathrm{J\,mol^{-1}K^{-1}}$
R_{rb}	Reaction rate of Boudouard reaction, $\mathrm{mol\,m^{-3}s^{-1}}$
ΔS	Molar entropy change of the electrochemical reactions, $\mathrm{J\,mol^{-1}}$
T_0	Ambient temperature, K
T_f	Operating temperature of the DC-SOFC, K
T_i (i=1,2,2s,3, 4,4s,5,6)	Temperatures of the working substance at operating state i, K
T	Temperature, K
u	Velocity vector, $\mathrm{m\,s^{-1}}$
V_f	Output voltage, V
V_{act}	Activation overpotential, V
V_{ohm}	Ohmic overpotential, V
y_j	Mole fraction of component j
Greek letters	
α	Electron transfer coefficient,
δ	Stefan-Boltzmann constant, $\mathrm{W\,m^{-2}K^{-4}}$
ε_{rc}	Recuperator coefficient
ε_h	Hot side coefficient
ε_L	Cold side coefficient
ζ	Emissivity of the DC-SOFC
η	Efficiency of the hybrid system
η_c	Compression efficiency
η_e	Expansion efficiency
η_f	Efficiency of the DC-SOFC
λ_{eff}	Effective heat conductivity, $\mathrm{W\,m^{-1}K^{-1}}$
μ	Dynamic viscosity of fluid, Pa s
ρ	Density, $\mathrm{Kg\,m^{-3}}$
σ^{eff}	Effective conductivity, $\mathrm{S\,m^{-1}}$
ϕ	Potential, V
Subscripts	
D	Point D
f	Fuel cell
j	Species (CO_2, CO, O_2)
P	Power
m	Maximum
Abbreviations	
DC-SOFC	Direct carbon solid oxide fuel cell
DCFC	Direct carbon fuel cell

343

344

345 **References**

346 [1] Lucia U. Overview on fuel cells. Renew. Sustain. Energy Rev. 2014; 30: 164-169.

347 [2] Sharaf O Z, Orhan M F. An overview of fuel cell technology: Fundamentals and
348 applications. Renew. Sustain. Energy Rev. 2014; 32: 810-853.

349 [3] Mekhilef S, Saidur R, Safari A. Comparative study of different fuel cell technologies.
350 Renew. Sustain. Energy Rev. 2012; 16: 981-989.

351 [4] Mond L, Langer C. A new form of gas battery. Proceedings of the Royal Society of London
352 1889; 46: 296-304.

353 [5] Kouchachvili L, Ikura M. Performance of direct carbon fuel cell. Int. J. Hydrogen Energy
354 2011; 36: 10263-10268.

355 [6] Park S, Vohs J M, Gorte R J. Direct oxidation of hydrocarbons in a solid-oxide fuel cell.
356 Nature 2000; 404: 265.

357 [7] Giddey S, Badwal S P S, Kulkarni A, Munnings C. A comprehensive review of direct carbon
358 fuel cell technology. Prog. Energy Comb. Sci. 2012; 38(3): 360-399.

359 [8] Cao D, Sun Y, Wang G. Direct carbon fuel cell: fundamentals and recent developments. J.
360 Power Sources 2007; 167: 250-257.

361 [9] Li C, Shi Y, Cai N. Mechanism for carbon direct electrochemical reactions in a solid oxide
362 electrolyte direct carbon fuel cell. J. Power Sources 2011; 196: 754-763.

363 [10] Guo L, Calo J M, DiCocco E, Bain E. Development of a low temperature, molten
364 hydroxide direct carbon fuel cell. Energy and Fuels 2013; 27: 1712-1719.

365 [11] Bai Y, Liu Y, Tang Y, Xie Y, Liu J. Direct carbon solid oxide fuel cell—a potential high
366 performance battery. Int. J. Hydrogen Energy 2011; 36: 9189-9194.

367 [12] Dudek M, Tomczyk P. Composite fuel for direct carbon fuel cell. Catal. Today 2011; 176:
368 388-392.

369 [13] Dudek M, Tomczyk P, Socha R, Hamaguchi M. Use of ash-free “Hyper-coal” as a fuel for

a direct carbon fuel cell with solid oxide electrolyte. Int. J. Hydrogen Energy 2014; 39: 12386-12394.

[14] Skrzypkiewicz M, Lubarska-Radziejewska I, Jewulski J. The effect of Fe_2O_3 catalyst on direct carbon fuel cell performance. Int. J. Hydrogen Energy 2015; 40: 13090-13098.

[15] Xu H, Chen B, Liu J, Ni Meng. Modeling of direct carbon solid oxide fuel cell for CO and electricity cogeneration. Appl. Energy 2016; 178: 353-362.

[16] Xiao J, Han D, Yu F, Zhang L, Liu J, Zhan Z, Zhang Y, Dong P. Characterization of symmetrical SrFe 0.75 Mo 0.25 O 3− δ electrodes in direct carbon solid oxide fuel cells. J. Alloy. Comp. 2016; 688: 939-945.

[17] Xu H, Chen B, Zhang H, Kong W, Liang B, Ni Meng. The thermal effect in direct carbon solid oxide fuel cells. Appl. Therm. Eng. 2017; 118: 652-662.

[18] Xie Y, Tang Y, Liu J. A verification of the reaction mechanism of direct carbon solid oxide fuel cells. J. Solid State Electrochem. 2013; 17: 121-127.

[19] Tang Y, Liu J, Sui J. A novel direct carbon solid oxide fuel cell. ECS Trans. 2009; 25: 1109-1114.

[20] Xu H, Chen B, Tan P, Zhang H, Yuan J, Irvin J T S, Ni Meng. Performance improvement of a direct carbon solid oxide fuel cell through integrating an Otto heat engine. Energy Convers. Manage. 2018; 165: 761-770.

[21] Xu H, Chen B, Tan P, Zhang H, Yuan J, Liu J, Ni Meng. Performance improvement of a direct carbon solid oxide fuel cell system by combining with a Stirling cycle. Energy 2017; 140: 979-987.

[22] Zhao M, Zhang H, Hu Z, Zhang Z, Zhang J. Performance characteristics of a direct carbon fuel cell/thermoelectric generator hybrid system. Energy Convers. Manage. 2015; 89: 683-689.

[23] Wang Y, Cai L, Liu T, Wang J, Chen J. An efficient strategy exploiting the waste heat in a solid oxide fuel cell system. Energy 2015; 93: 900-907.

395 [24] Yang Z, Peng W, Liao T, Zhao Y, Lin G, Chen J. An efficient method exploiting the waste
396 heat from a direct carbon fuel cell by means of a thermophotovoltaic cell. Energy Convers.
397 Manage. 2017; 149: 424-431.
398 [25] Açıkkalp E. Performance analysis of irreversible solid oxide fuel cell–Brayton heat engine
399 with ecological based thermo-environmental criterion. Energy Convers. Manage. 2017; 148:
400 279-286.
401 [26] Chen L, Zhang H, Gao S, Gao S, Yan H. Performance optimum analysis of an irreversible
402 molten carbonate fuel cell–Stirling heat engine hybrid system. Energy 2014; 64: 923-930.
403 [27] Açıkkalp E. Performance analysis of irreversible molten carbonate fuel cell–Braysson heat
404 engine with ecological objective approach. Energy Convers. Manage. 2017; 132: 432-437.
405 [28] Ahmadi M H, Jokar M A, Ming T, Feidt M, Pourfayaz F, Astaraei F R. Multi-objective
406 performance optimization of irreversible molten carbonate fuel cell–Braysson heat engine and
407 thermodynamic analysis with ecological objective approach. Energy 2018; 144: 707-722.
408 [29] Açıkkalp E. Ecologic and Sustainable Objective Performance Analysis of a Molten
409 Carbonate Fuel Cell–Heat Engine Hybrid System. J. Energy Eng. 2017; 143: 04017062.
410 [30] Acikkalp E, Ahmadi M H. Parametric Investigation of Phosphoric Acid Fuel Cell -
411 Thermally Regenerative Electro Chemical Hybrid System. J. Clean. Prod. 2018.
412 [31] Mehrpooya M, Dehghani H, Moosavian S M. Optimal design of solid oxide fuel cell,
413 ammonia-water single effect absorption cycle and Rankine steam cycle hybrid system. J. Power
414 Sources 2016: 107-123.
415 [32] Jokar M A, Ahmadi M H, Sharifpur M, Meyer J P, Pourfayaz F, Ming T. Thermodynamic
416 evaluation and multi-objective optimization of molten carbonate fuel cell-supercritical CO_2
417 Brayton cycle hybrid system. Energy Convers. Manage. 2017; 153: 538-556.
418 [33] Açıkkalp E. Ecologic and sustainable objective thermodynamic evaluation of molten
419 carbonate fuel cell–supercritical CO_2 Brayton cycle hybrid system. Int. J. Hydrogen Energy

2017; 42:6272-6280.

[34] Dostal V, Hejzlar P, Driscoll M J. High-performance supercritical carbon dioxide cycle for next-generation nuclear reactors. Nucl. Technol. 2006; 154: 265-282.

[35] Le Roux W G, Bello-Ochende T, Meyer J P. The efficiency of an open-cavity tubular solar receiver for a small-scale solar thermal Brayton cycle. Energy Convers. Manage. 2014; 84: 457-470.

[36] Huang Y, Lin Q, Liu H, Ni M, Zhang X. Evaluation of the waste heat and residual fuel from the solid oxide fuel cell and system power optimization. Int. J. Heat Mass Transfer 2017; 115: 1166-1173.

[37] Pirkandi J, Mahmoodi M, Ommian M. An optimal configuration for a solid oxide fuel cell-gas turbine (SOFC-GT) hybrid system based on thermo-economic modelling. J. Clean. Prod. 2017: 375-386.

[38] Sánchez D, de Escalona J M M, Chacartegui R, Chacartegui R, Munoz A, Sanchez T. A comparison between molten carbonate fuel cells based hybrid systems using air and supercritical carbon dioxide Brayton cycles with state of the art technology. J. Power Sources 2011; 196: 4347-4354.

[39] Yang Z, Xu H, Chen B, Tan P, Zhang H, Ni M. Numerical modeling of a cogeneration system based on a direct carbon solid oxide fuel cell and a thermophotovoltaic cell. Energy Convers. Manage. 2018; 171: 279-286.

[40] Xu H, Chen B, Tan P, Cai W, Wu Y, Zhang H, Ni M. A feasible way to handle the heat management of direct carbon solid oxide fuel cells. Appl. Energy 2018; 226: 881-890.

[41] Xu H, Chen B, Ni M. Modeling of Direct Carbon-Assisted Solid Oxide Electrolysis Cell (SOEC) for Syngas Production at Two Different Electrodes. J Electrochem. Soc. 2016; 163: F3029-F35.

[42] Zhang X, Su S, Chen J, Zhao Y, Brandon N. A new analytical approach to evaluate and

445 optimize the performance of an irreversible solid oxide fuel cell-gas turbine hybrid system. Int.
446 J. Hydrogen Energy 2011; 36:15304-15312.
447 [43] Ahmadi M H, Ahmadi M A, Pourfayaz F, Bidi M. Thermodynamic analysis and
448 optimization for an irreversible heat pump working on reversed Brayton cycle. Energy Convers.
449 Manage. 2016; 110: 260-267.
450 [44] Ust Y, Sahin B, Kodal A, Akcay I H. Ecological coefficient of performance analysis and
451 optimization of an irreversible regenerative-Brayton heat engine. Appl. Energy 2006; 83: 558-
452 572.
453 [45] Xie Y, Cai W, Xiao J, et al. Electrochemical gas–electricity cogeneration through direct
454 carbon solid oxide fuel cells. J. Power Sources, 2015, 277: 1-8.
455 [46] Chen L, Ding Z, Zhou J, Wang W, Sun F. Thermodynamic performance optimization for
456 an irreversible vacuum thermionic generator. Eur. Phys. J. Plus 2017; 132: 293.
457 [47] Yilmaz T. A new performance criterion for heat engines: efficient power. J. Energy Inst.
458 2006; 79: 38-41.
459 [48] Ahmadi M H, Ahmadi M A, Pourfayaz F. Thermal models for analysis of performance of
460 Stirling engine: A review. Renew. Sustain. Energy Rev. 2017; 68: 168-184.
461
462

463 **List of Table**

467

468 Table 1.
469

Chemical reaction	
Boudouard reaction	$C + CO_2 = 2CO$
Reaction rate of Boudouard reaction (mol m^{-3} s^{-1})	$R_{rb} = k_{rb} C_{CO_2} \exp(-E_{rb} / RT)$
Electrochemical reaction	
Anode electrochemical reaction	$2CO + 2O^{2-} \rightarrow 2CO_2 + 4e^-$
Cathode electrochemical reaction	$O_2 + 4e^- \rightarrow 2O^{2-}$
Output voltage (V)	$V_f = E_{CO} - V_{act} - V_{ohm}$
Equilibrium potential (V)	$E_{CO} = E^0_{CO} + \frac{RT}{2F} \ln\left[\frac{p^L_{CO}\left(p^L_{O_2}\right)^{0.5}}{p^L_{CO_2}}\right]$
Standard potential (V)	$E^0_{CO} = 1.46713 - 0.000452T$
Butler-Volmer equation	$i_f = i_0\left\{\exp\left(\frac{\alpha n F V_{act}}{RT}\right) - \exp\left[\frac{(1-\alpha) n F V_{act}}{RT}\right]\right\}$
Ohmic potential (V)	$\nabla(\emptyset) = \frac{\sigma^{eff}}{i}$
Species transport	
Extended Fick's model	$N_i = -\frac{1}{RT}\left(\frac{B_0 y_j p}{\mu}\frac{\partial p}{\partial z} - D_j^{eff}\frac{\partial(y_j p)}{\partial z}\right) \quad (j = 1, \ldots, m)$
Momentum conservation	
Navier-Stokes equation	$\rho\frac{\partial u}{\partial t} + \rho u \nabla u = -\nabla p + \nabla\left[\mu\left(\nabla u + (\nabla u)^T\right) - \frac{2}{3}\mu\nabla u\right]$
Heat transfer	
General heat balance equation	$\rho C_p u \cdot \nabla T + \nabla \cdot \left(-\lambda_{eff}\nabla T\right) = \dot{q}$

470
471

472 Table 2.

Parameters	**Value or expression**
Ionic conductivity, $\mathrm{S\,m^{-1}}$	
Gadolinium doped ceria (GDC)	$(100/T)10^{(6.66071-5322.92/T)}$
Yttrium stabilized zirconium (YSZ)	$33400\exp(-10300/T)$
Electronic conductivity, $\mathrm{S\,m^{-1}}$	
Ag	$\frac{1.59e^{8}}{0.0038T-0.1134}$
Porosity	
Cathode	0.46
Anode	0.46
Electrode volume fraction	
GDC	0.21
Ag	0.79
S_{TPB}	
Cathode layer,	2.14×10^{5}
Anode layer,	2.14×10^{5}
Tortuosity	
Cathode	3
Anode	3
Exchanger current density, $\mathrm{A\,m^{-2}}$	
CO	450
O_2	400
Charge transfer coefficient,	
CO	0.5
O_2	0.5
Equilibrium constant of Boudouard reaction k_{rb}, $\mathrm{s^{-1}}$	6×10^{13}
Activation energy of Boudouard reaction E_{rb}, kJ $\mathrm{mol^{-1}}$	248

473

474

475 Table 3

Parameters	**Value**
Compression efficiency, η_c	0.91
Expansion efficiency, η_e	0.94
Recuperator coefficient, ε_{rc}	0.98
Cold side coefficient, ε_L	0.90
Hot side coefficient, ε_h	0.90
Environment temperature, $T_0(\mathrm{K})$	300

476

477

478 **List of Figures**

501

Fig. 1.

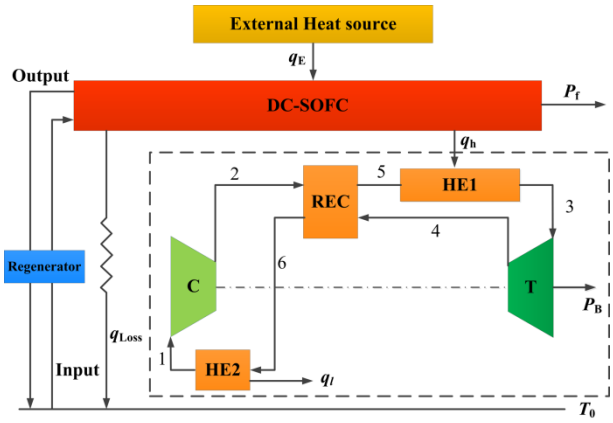
External Heat source
q_E
Output
DC-SOFC
P_f
q_h
2
REC
5
HE1
3
4
Regenerator
6
C
T
P_B
q_{Loss}
1
HE2
q_l
Input
T_0

505 Fig. 2.

506

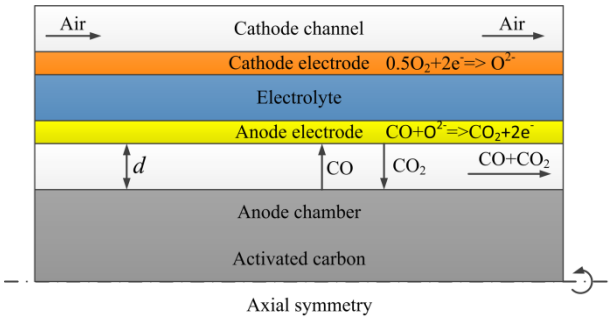

507

508 Fig. 3.

509

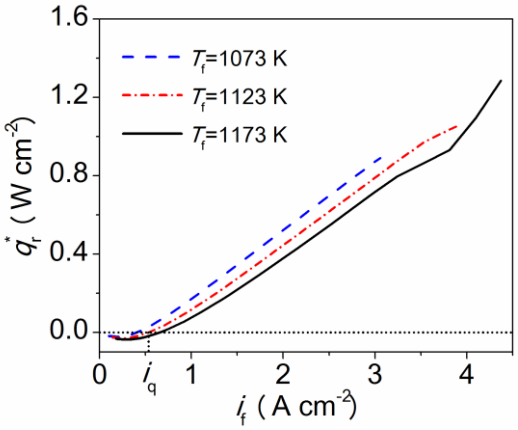

510

511 Fig. 4.

512

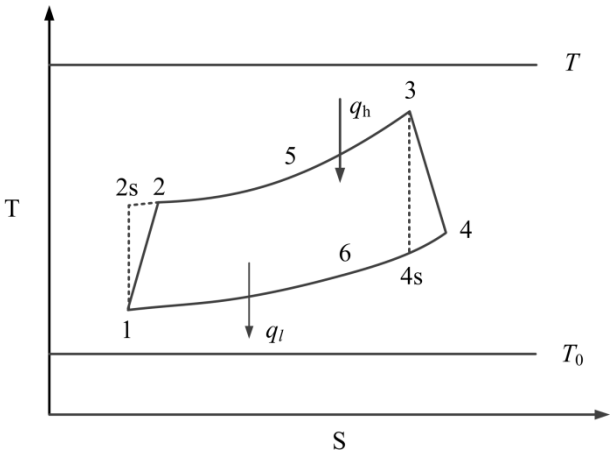

513

514 Fig. 5.

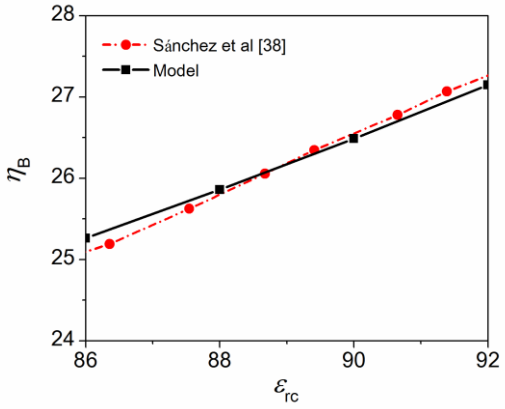

515
516

517 Fig. 6.

518

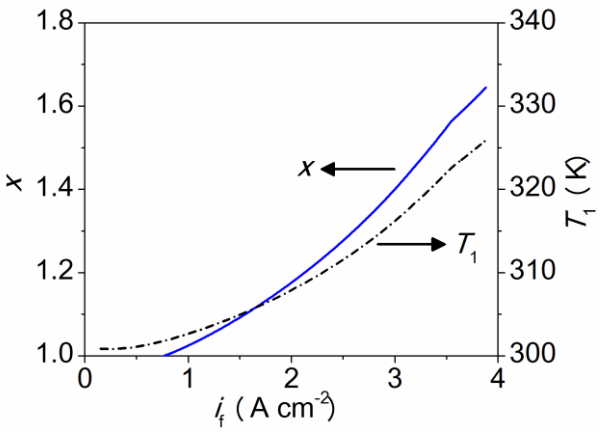

519

Fig. 7.

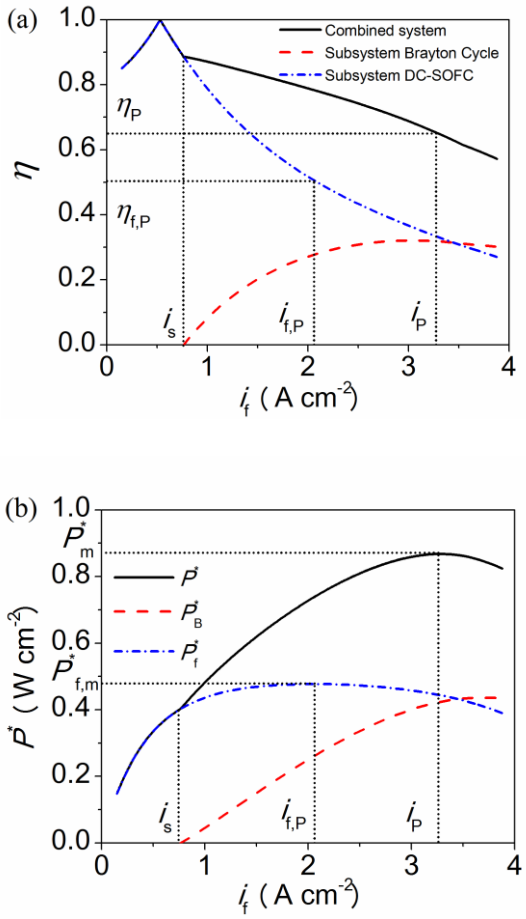
(a)
Combined system
Subsystem Brayton Cycle
Subsystem DC-SOFC
η_P
$\eta_{f,P}$
η
i_s
$i_{f,P}$
i_P
i_f (A cm^{-2})
(b)
P^*_m
P^*
P^*_B
P^*_f
$P^*_{f,m}$
P^* (W cm^{-2})
i_s
$i_{f,P}$
i_P
i_f (A cm^{-2})

524 Fig. 8.

525

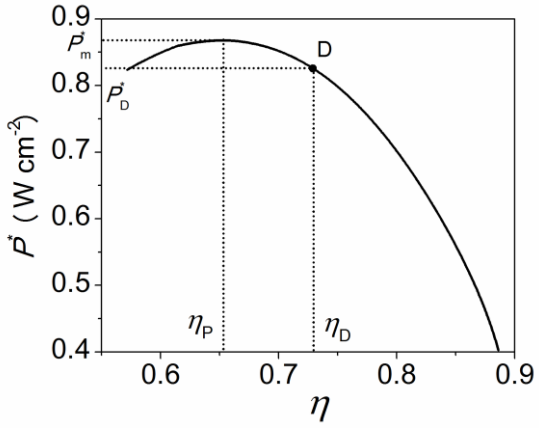

526

527 Fig. 9.

528

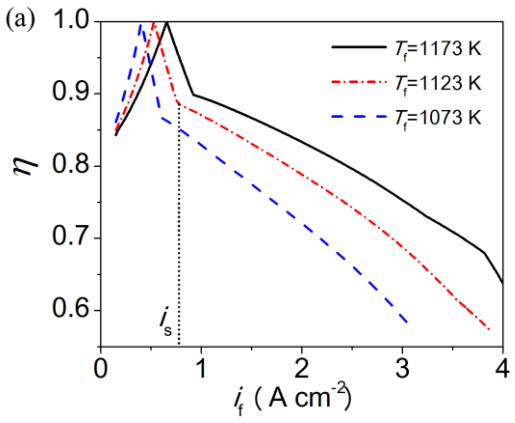

529

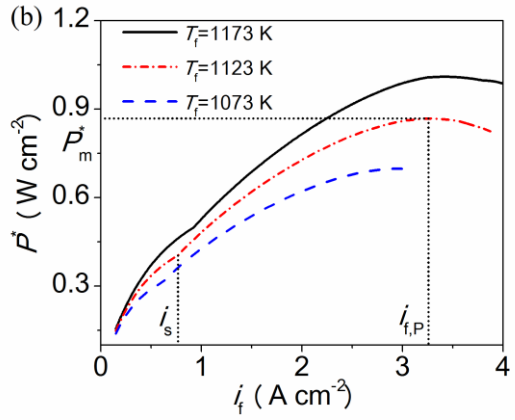

530

Fig. 10.

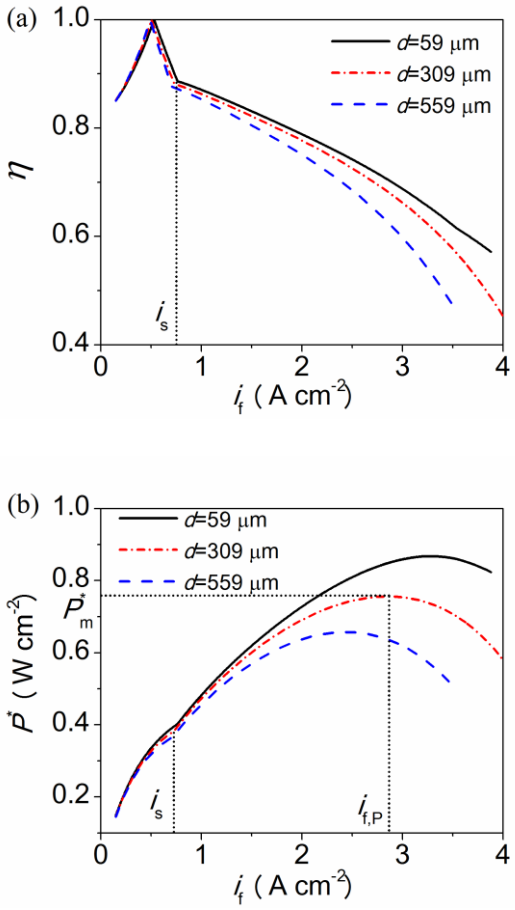
(a)
1.0
0.8
0.6
0.4
η
d=59 μm
d=309 μm
d=559 μm
i_s
0
1
2
3
4
i_f (A cm^{-2})
(b)
1.0
0.8
0.6
0.4
0.2
P^* (W cm^{-2})
P^*_m
d=59 μm
d=309 μm
d=559 μm
i_s
$i_{f,P}$
0
1
2
3
4
i_f (A cm^{-2})

535 Fig. 11.

536

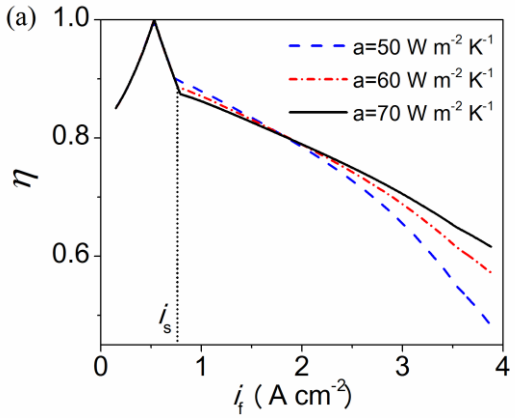

537

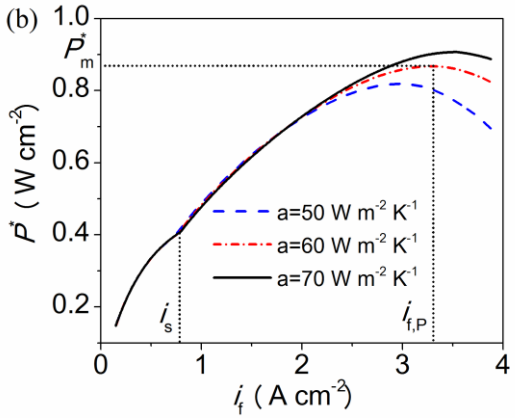

538

539 Fig. 12.

540

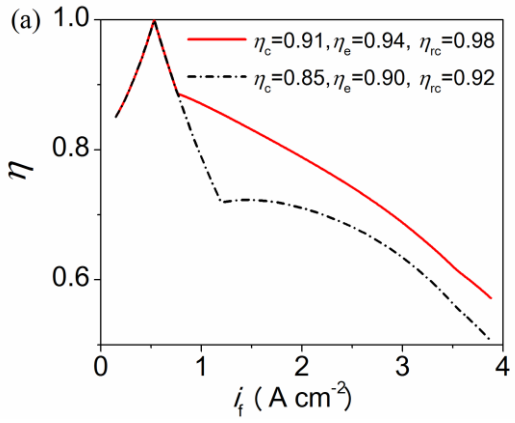

541

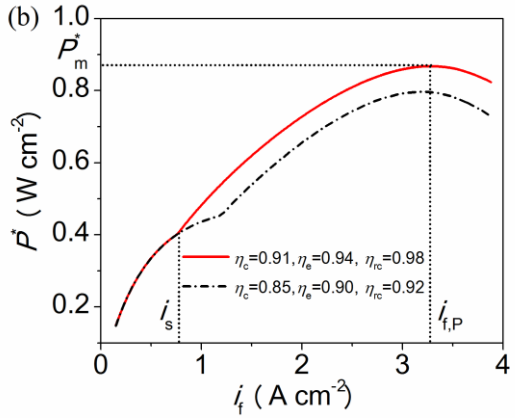

542

543 Fig. 13.

544